

Production of Molybdenum Trioxide Nanosheets by Liquid Exfoliation and their Application in High Performance Supercapacitors

Damien Hanlon^{1,2}, Claudia Backes^{1,2}, Thomas M Higgins^{1,2}, Marguerite Hughes^{1,2}, Arlene O'Neill^{1,2}, Paul King^{1,2}, Niall McEvoy,^{1,3} Georg S Duesberg,^{1,3} Beatriz Mendoza Sanchez^{1,3}, Henrik Pettersson^{1,2}, Valeria Nicolosi^{1,2,3} and Jonathan N Coleman^{1,2*}

¹*CRANN & AMBER Research Centres, Trinity College Dublin, Dublin 2, Ireland*

²*School of Physics, Trinity College Dublin, Dublin 2, Ireland*

³*School of Chemistry, Trinity College Dublin, Dublin 2, Ireland*

*colemaj@tcd.ie

ABSTRACT:

Here we demonstrate a simple method to exfoliate layered molybdenum trioxide (MoO_3) crystallites to give multi-layer MoO_3 nanosheets dispersed in solvents. Exfoliation is achieved by sonicating MoO_3 powder in the presence of suitable solvents followed by centrifugation to remove undispersed material. This procedure works well in a range of solvents with Hildebrand solubility parameters close to $21 \text{ MPa}^{1/2}$, and is consistent with the predictions of classical solubility theory. We have fully optimised this process and demonstrated methods to separate the resultant nanosheets by size. Raman spectroscopy suggests the exfoliation process does not damage the MoO_3 . This is supported by measurements which show reaggregated nanosheets to display very similar photoluminescence to bulk MoO_3 . However, the dispersed nanosheets had distinctly different photoluminescence indicating a decoupling of the monolayers on exfoliation. We have used liquid exfoliated MoO_3 to prepare supercapacitor electrodes which had relatively low capacitance ($\sim 2 \text{ F/g}$ at 10 mV/s), due to the low electrical conductivity of the MoO_3 . However, addition of carbon nanotubes beyond the percolation threshold yielded a 100-fold increase in capacitance. Some MoO_3 /nanotube composites displayed capacitances as high as 540 F/g at 0.1 mV/s . This is the first example of solvent exfoliation of a layered metal oxide. We believe this work opens the way to liquid exfoliation of a wide range of layered compounds leading to an array of new solution processed 2D materials.

Keywords: sonication, delamination, thermodynamics, layered, multilayer, ultracapacitor

Introduction

Since the first papers to describe the electrical properties of monolayer graphene appeared almost a decade ago,¹ the study of two-dimensional (2D) nano-materials has become one of the most vibrant areas of materials science. In the early days, much of the excitement was driven by the unprecedented properties of graphene itself.^{2, 3} However, more recently awareness has grown that a wide range of 2D materials can be envisaged.⁴ Such materials are not normally found in a 2D form, but consist of planar nanosheets stacked together to form layered crystals. These compounds can be grouped into families such as the metal chalcogenides,⁵⁻⁷ the metal oxides^{8, 9} and the phyllosilicates¹⁰ which include well-known materials such as MoS₂, layered MnO₂ and mica as well as less familiar forms such as VSe₂, MoO₃ and kaolinite. The large number of layered materials provides scope for the production an equally wide range of 2D systems with a very broad pallet of properties.

While 2D materials can be produced by micromechanical cleavage of layered crystals^{11, 12} or bottom-up^{13, 14} growth methods such as chemical vapour deposition, these methods are unsuitable for many practical applications. A number of areas, especially those involving the formation of thin films or composites, require exfoliation methods which give relatively large quantities of materials in a processable form. In such cases, the most appropriate method for producing 2D materials is liquid exfoliation.⁴ This technique is extremely useful because it gives liquid-suspended nanosheets which can then be processed into films, composites or other structures. It has proven very successful in exfoliating a wide range of layered crystals including graphite, metal chalcogenides and metal oxides.⁴

While a number of distinct liquid exfoliation technologies exist,⁴ probably the simplest is liquid phase exfoliation which involves sonicating the layered crystals in certain stabilising liquids.^{4, 15-17} The sonic energy tends to exfoliate¹⁸ the crystals to give nanosheets stabilised against aggregation by interaction with the liquid.¹⁵ The stabilising liquids can be certain solvents^{16, 17, 19-30} or solvent blends^{31, 32}, aqueous surfactant solutions³³⁻³⁶ or polymer solutions.^{37, 38} Both surfactant- and polymer-stabilisation are due to repulsive forces between adjacent polymer- or surfactant-coated nanosheets. Solvent stabilisation is simpler – it is believed that solvents with the correct surface-energy or solubility parameters bind by van der Waals interactions to nanosheets with strengths that are similar to the inter-nanosheet binding strength.³⁹ This dramatically reduces the net energy cost of exfoliation. These

mechanisms are not specific to any particular type of 2D material which implies that the approach is general and can be adopted for a broad host of layered compounds. Indeed, this has already demonstrated for graphene, BN, MoS₂, WS₂ and a variety of other transition metal dichalcogenides (TMDs).^{4, 15, 16}

Liquid phase exfoliation has a number of advantages in that it is quick, easy, insensitive to environmental conditions and amenable to scale up. It produces nanosheets which are dispersed in liquid and so can be easily processed into a range of structures including films and composites. Materials produced and processed in this way have been applied in a number of fields such as fabrication of liquid crystal displays¹⁹, mechanically reinforced composites,^{40, 41} lithium ion batteries,⁴² photodetectors,⁴³ and printed micro-supercapacitors⁴⁴ to name but a few. However, this method has not been extended beyond the limited number of materials described above. As mentioned earlier, there are numerous layered materials,⁴ many of which are potentially amenable to solvent (or surfactant or polymer) based exfoliation. In order to exploit the potential of layered compounds to become the source of a diverse array of 2D nanosheets, it will be necessary to demonstrate that many different types of layered materials can be exfoliated in liquids – ideally by solvent exfoliation.

Layered metal oxides represent a rich class of layered materials with a range of interesting dielectric, electronic and electrochemical properties.⁹ It is well-known that layered metal oxides can be exfoliated by ion-exchange based exfoliation.^{8, 9, 45} The resultant exfoliated materials have been studied in a range of applications from high- κ dielectrics to magneto-optics to energy storage devices.^{8, 9} Ion exchange methods of exfoliation are usually used because many layered oxides tend to be found as mixed valence compounds as so require the presence of charge balancing counterions which reside between the layers.^{4, 9} Replacement of these counterions by larger ones such as tetrabutylammonium ions increases the inter-layer distances between the sheets and enables their exfoliation.^{8, 9} However, some metal oxides, such as MoO₃, occur naturally as single valence compounds. Such compounds cannot be exfoliated by ion-exchange methods. In addition, as interest in 2D materials grows, it is likely that methods will be found to synthesise layered oxides, which previously had been found only in mixed valence form, as single valence compounds. Thus, it is worth attempting to apply liquid phase exfoliation techniques to single valence layered oxides with

the aim of demonstrating the possibility of producing stably suspended nanosheets at reasonably high concentration.

Here we identify MoO_3 as a promising candidate for solvent exfoliation (see figure 1A for structure). This material is a layered compound that occurs naturally as the mineral molybdenite. Bulk MoO_3 is commercially available and widely abundant. As such, it is used extensively as a catalyst and in the production of Mo metal. While the atoms within MoO_3 monolayers are bound together by chemical bonds, the inter-nanosheet interaction is dominated by van der Waals forces, implying this material to be suitable for liquid phase exfoliation.^{46, 47} Critically, MoO_3 is a single valence compound (*i.e.* a $4d_0$ Mo(VI) compound) consisting of uncharged layers without the need for counter ions.^{48, 49} This makes it suitable for exfoliation in appropriate solvents or indeed using surfactant or polymer solutions. This is particularly interesting, as ion exchange methods that have proven successful for other layered oxides, cannot be applied to MoO_3 . The ability to exfoliate this material is important, as nano-structured MoO_3 is expected to be a valuable component in a number of applications including electrodes in supercapacitors⁵⁰⁻⁵² and Li ion batteries.⁵³⁻⁵⁷ Equally important, successful exfoliation would demonstrate that these techniques can be extended beyond familiar materials such as graphene, BN and TMDs.

In this paper we demonstrate that solvent exfoliation can be applied to the layered oxide MoO_3 . The exfoliation of MoO_3 powder gives large quantities of nanosheets in a range of common solvents. We describe the optimisation of the exfoliation procedure and reveal that nanosheets of different sizes can be controllably produced. Raman and photoluminescence spectroscopy show the material to be undamaged by the exfoliation process and confirm the exfoliated nanosheets to have electronic properties distinct from those of the bulk. Finally, we demonstrate the formation of films of MoO_3 nanosheets. By adding small quantities of carbon nanotubes, these films can be fabricated into supercapacitor electrodes with a capacitance of up to 540 F/g.

RESULTS AND DISCUSSION

Solvent dependence

To investigate the possibility of solvent exfoliation of uncharged layered oxides such as molybdenum trioxide, we sonicated as-received MoO_3 powder in a broad range of solvents

(initial MoO₃ concentration, C_i = 1 mg/mL, sonication time, t_s = 15 mins) and centrifuged the resulting dispersions to remove any unexfoliated material. We note that the centrifugation regime must be carefully chosen (see methods) to avoid effects due to variation of viscosity among solvents (centrifugation time, t_{CF} = 50 min, centrifugation rate = 1.5 krpm, *i.e.* ~240g). Transmission electron microscopy (TEM) characterisation showed all dispersions to be rich in 2D nanosheets such as the one displayed in figure 1B inset. We recorded optical absorption spectra for all dispersions and take the measured absorbance per cell length (A/l) at 375 nm as a metric for dispersed concentration. We found A/l to vary over 3-4 orders of magnitude for the solvents studied. Shown in figure 1A is a graph of measured A/l *versus* the Hildebrand solubility parameter of the solvent, δ_s. This parameter is defined as the square root of the solvent cohesive energy density⁵⁸ and is well known to influence solubility for both molecular⁵⁸⁻⁶⁰ and nanoscale solutes.^{16, 17, 22, 39, 61} The experimental results display a well-defined peak centred at δ_s ~ 20-21 MPa^{1/2}. We note that the best performing solvents were *N*-cyclohexyl-2-pyrrolidone (CHP), cyclohexanone and *N*-methyl-2-pyrrolidone (NMP) with δ_s = 20.5, 20.3 and 23.0 MPa^{1/2} respectively.

Classical solution thermodynamics shows that, in the simplest case, the saturated concentration of 2D solutes is approximately given by³⁹

$$C \propto \exp \left[-\frac{v_{NS}}{3kT} (\delta_s - \delta_{NS})^2 \right] \quad (1)$$

where δ_{NS} represents the Hildebrand parameter of the 2D solute, v_{NS} represents the molecular volume of the solute while the factor of three stems from the solute dimensionality.³⁹ We note that, in principle, this approach is not strictly applicable to nanoscale solutes such as graphene, MoS₂ or MoO₃. It is overly simplistic with a number of other models providing a better physical description at the molecular scale.^{62, 63} However, in practice this approach (and related ones based on surface energy and Hansen solubility parameters^{16, 17, 22, 23, 32, 61, 64-68}) supplies an extremely good framework for analysing solubility and predicting suitable solvents. Its main weakness is that, in the case of nanoscale solutes, values of \bar{v}_{NS} extracted from width of the C *versus* δ_s peak rarely agree with the theoretical values.^{22, 69}

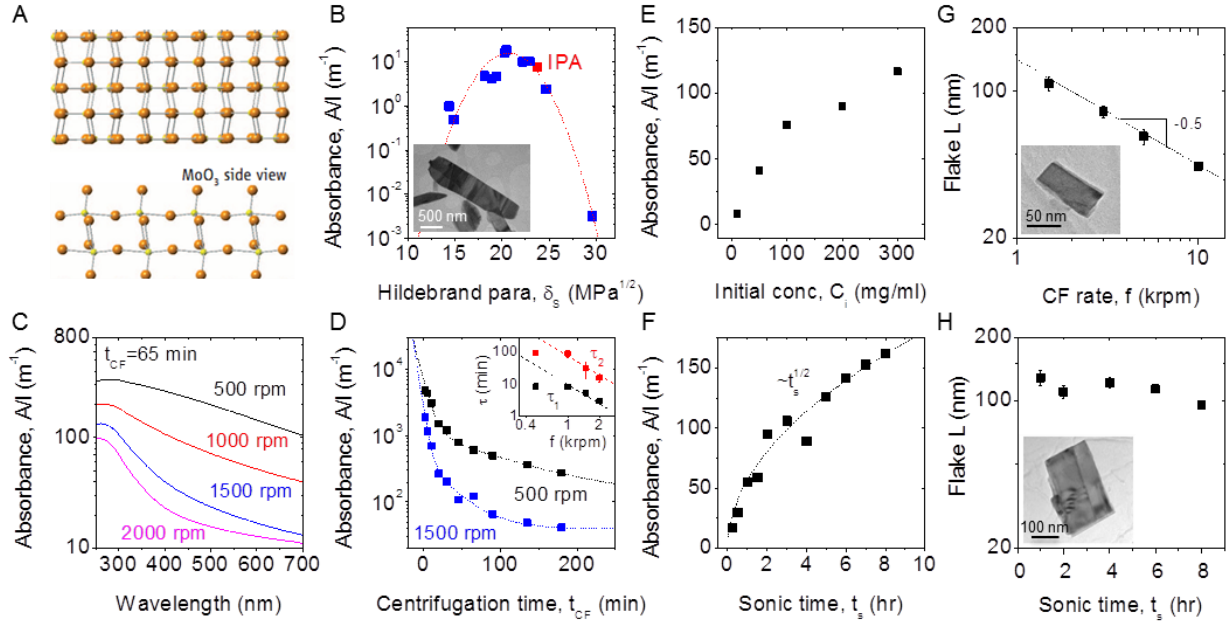


Figure 1: A) Structure of MoO₃ from above, viewing the a-c plane (top) and from the side, viewing the b-c plane (bottom). B) Dispersed concentration of MoO₃ as represented by optical absorbance (375 nm) divided by cell length, A/l, plotted *versus* solvent Hildebrand parameter, δ_s . The dashed line is a fit to equation 1. The dispersions in B had initial concentration of C_i=1 mg/mL, each were sonicated for t_s=15 min and centrifuged at f=1.5 krpm for t_{CF}=50 min. Inset: TEM image of an NMP-exfoliated MoO₃ nanosheet. C) Optical absorbance spectra for dispersions prepared at different centrifugation rates in isopropanol (C_i=50 mg/mL, t_s=2 hrs, t_{CF}=65 min). D) Optical absorbance (375 nm) plotted as a function of centrifugation time for dispersions prepared at two centrifugation rates, 500 and 1500 rpm (isopropanol, C_i=50 mg/mL, t_s=2 hrs). The lines are fits to equation 2. Inset: Time constants plotted as a function of centrifugation rate, f. The lines indicate $\tau \propto f^{-2}$. E) Optical absorbance (375 nm) plotted *versus* initial concentration (IPA, t_s=2 hrs, f=1.5 krpm, t_{CF}=110 min). F) Optical absorbance (375 nm) plotted *versus* sonication time (IPA, C_i=300 mg/mL, f=1.5 krpm, t_{CF}=110 min). G) Mean nanosheet length measured by TEM as a function of centrifugation rate (C_i=50 mg/mL, t_s=5 hrs, t_{CF}=110 min). Inset: Typical flake (3 krpm). H) Flake length plotted *versus* sonication time (C_i=300 mg/mL, f=1.5 krpm, t_{CF}=2 hrs). Inset: Typical flake (t_s=5 hrs).

Fitting equation 1 to the data in figure 1B, gives extremely good agreement and shows $\delta_{NS} = 20.7 \text{ MPa}^{1/2}$ for MoO₃. This compares to reported values for graphene, BN, WS₂, MoS₂,

MoSe₂ and MoTe₂ which all fell in the range 21-22.5 MPa^{1/2}.^{16, 22, 23} This data implies that the exfoliation and stabilisation of MoO₃ occurs in a manner similar to other layered materials, consistent with classical solubility theory. This is of great interest, as it demonstrates that the solvent exfoliation approach can be extended beyond graphene, BN and TMDs. It is very likely that other layered oxides or indeed 2-dimensional materials of different families such as the III-VIs (GaS, InSe etc) or metal halides,⁴ can be exfoliated in this way.

The data presented in figure 1B allows us to choose from a range of solvents when exfoliating MoO₃. For the subsequent study, we focus on 2-propanol (IPA) rather than the solvents quoted above, simply because it is beneficial to work with due to its low toxicity and boiling point. However, to optimise the exfoliation/dispersion procedure, it is necessary to determine the effect of processing parameters such as centrifugation (CF) conditions, initial MoO₃ concentration and sonication time on the properties of MoO₃/IPA dispersions.

Processing parameters

We initially performed experiments to assess the effect of CF rate and time on the concentration of MoO₃ dispersions. The dispersions in IPA were sonicated ($t_s = 2$ hrs, $C_i = 50$ mg/ml) and then centrifuged at different speeds (expressed as rotation rate, f) for a range of times. As shown in figure 1C, optical absorbance spectra depend strongly on the centrifugation speed (for fixed CF time, $t_{CF} = 65$ min). At low rotation rate, the spectral features are superimposed on a broad background generally attributed to light scattering.^{16, 70} When increasing the centrifugation velocities, both scattering background and concentration are reduced as larger aggregates are removed from the dispersion. Similar behaviour (not shown) can be observed for dispersions centrifuged at a fixed rate for various times with the background decreasing as CF time is increased. We can summarise this behaviour by plotting the absorbance (375 nm) *versus* CF time for different CF rates in figure 1D. In analogy to the behaviour previously observed for sedimentation of graphite/graphene dispersions, we can fit these curves with a bi-exponential decay,⁷¹ where the decaying components represent two unstable species in our system in addition to a stable component. The unstable species can be separated into a slowly sedimenting phase and a fast sedimenting phase.¹⁸ These can be associated with large, unexfoliated grains of powder sedimenting quickly and mid-sized exfoliated nanosheets which would sediment more slowly.^{18, 72} Within this scheme, the absorbance decays with time as⁷¹

$$(A/l) = (A/l)_0 + (A/l)_1 e^{t/\tau_1} + (A/l)_2 e^{t/\tau_2} \quad (2)$$

where $(A/l)_0$ represents the absorbance of the stable phase while $(A/l)_1$ and $(A/l)_2$ represent the initial absorbance of the fast and slow sedimenting phases, respectively. In addition, τ_1 and τ_2 represent the sedimentation time constants of these phases, respectively. We found short and long time constants in the range 2-10 and 10-100 min, respectively (figure 1D inset). Empirically, the time constants decreased roughly as $\tau \propto f^{-2}$, equivalent to $\tau \propto F^{-1}$ where F is the centrifugal force during centrifugation. Once the time constants are known, we can estimate the optimal centrifugation time which will depend on specific requirements. For example, if one wants to remove all unexfoliated powder but retain all dispersed nanosheets (stable and unstable, *i.e.* phases 0 and 2), then the required centrifugation times is $t_{CF} = 3\tau_1$ (3 time constants is the time taken for an exponential to decay by 95%). However, if one wants to remove all unstable material but retain all stable nanosheets then $t_{CF} \geq 3\tau_2$. In addition, one must choose the CF rate in such a way that it gives a good balance between the concentration of the final dispersion and the CF time required. In order to produce dispersions of stable MoO₃ nanosheets, we chose a combination of 1.5 krpm (~240g) and $t_{CF} = 110$ mins. This results in a stable concentration characterised by $A/l = 109 \text{ m}^{-1}$.

With knowledge of the centrifugation velocities and times required for the production of stable dispersions, it is important to maximise the dispersed concentration. To address this, we prepared dispersions for a range of initial MoO₃ concentrations (IPA, $t_s = 2$ hrs, $f = 1.5$ krpm (~240g), $t_{CF} = 110$ mins). We plot the absorbance after CF *versus* C_i in figure 1E, observing a linear increase in the MoO₃ concentration up to $C_i = 100$ mg/mL. Above this, the system begins to saturate, as the limit of the concentration of the solute stably dispersible in IPA is approached. For the following investigations, we fixed the initial concentration at 300 mg/mL.

It is also important to assess the effect of sonication time. We sonicated MoO₃ powder in a large volume of IPA (100 mL), removing aliquots at various sonication times which were subsequently centrifuged ($C_i = 300$ mg/mL, 1.5 krpm (~240g), $t_{CF} = 110$ mins). We found the dispersed concentration (expressed as A/l) to increase sub-linearly with sonication time (figure 1F), consistent with $C \propto t_s^{1/2}$ as has previously been observed for a number of

systems.^{18, 24, 72, 73} To allow the maximum throughput, we have settled on a 5 h sonication period.

We don't expect the solvent used, the initial concentration or the centrifugation time (so long as only stable nanosheets are retained: $t_{CF} \geq 3\tau_2$) to have any significant effect on the dispersed nanosheet size. However, the lateral size of the nanosheets will certainly depend on the sonication time and the centrifugation rate. To assess this, we performed TEM analysis on dispersions prepared while independently varying CF rate and sonication time, but keeping the other variables constant. Shown in figure 1G inset is a TEM image of a typical MoO₃ nanosheet (3 krpm, ~950g). We measured the mean flake length, L, for a number of CF rates (figure 1G). The flake length decreases from ~100 nm to ~40 nm as the rate is increased from 1.5 to 10 krpm (~240g to 10500g). Interestingly, the nanosheet length falls off as $f^{-1/2}$, equivalent to $F^{-1/4}$. In order to probe whether nanosheet size changed with increasing sonication times as a result of potential sonication induced scission,⁷⁴ the mean flake lengths were measured for a number of sonication times (figure 1H). No significant reduction in flake sizes was recorded up to sonication times of 8 h suggesting that sonication induced scission is not occurring over the range of sonication times studied.

It is worth noting that these flakes are small relative to other exfoliated layered materials. Under similar centrifugation conditions, solvent-exfoliated graphene and MoS₂ nanosheets have been produced with mean lengths of ~1 μm and ~0.3 μm respectively.^{16, 24} We argue that, even though we do not observe sonication induced scission occurring, it does in fact control the observed MoO₃ nanosheet size.⁷⁴ Lucas et al.⁷⁴ have shown that, after extensive sonication, the length of dispersed carbon nanotubes reaches a terminal value, L_t , which is related to nanotube strength, σ_B , as $L_t = k\sigma_B^{1/2}$, where k is a constant. We have already demonstrated that the size of solvent exfoliated graphene and MoS₂ nanosheets is consistent with this mechanism.⁷⁰ It is possible that this terminal length is reached early in the experiment described in figure 1H, perhaps before $t_s=2$ hrs. For this to be the case, the MoO₃ itself (*i.e.* the intra-layer bonds) would have to be relatively weak. Using data for graphene flakes, sonicated in NMP, which appear to have reached terminal length ($L_t \sim 800$ nm, $\sigma_B \sim 130$ GPa),^{24, 75} we estimate: $k \sim 2 \times 10^{-12}$ Pa^{-1/2}m. Assuming the terminal length for MoO₃ is ~100 nm (figure 1H), this predicts the strength of MoO₃ nanosheets to be ~2.5 GPa. This is considerably smaller than the accepted values of graphene and MoS₂ (130 and 23 GPa),^{75, 76}

but larger than that of mica (250 MPa).⁷⁷ In fact the strength of MoO₃ may be limited by the presence of oxygen vacancies (see below). Thus, we believe sonication-induced scission to be a potential source to explain the small mean size of dispersed MoO₃ nanosheets.

In summary, sonication of MoO₃ powder in IPA can give reasonable quantities of stably dispersed small (~100 nm) nanosheets within moderate preparation times. Optimised processing parameters are as follows: C_i= 300 mg/mL, t_s= 5 hrs, f=1.5 krpm (~240g), t_{CF}=110 mins. Processing using these conditions gives a dispersion with A/l=109 m⁻¹. By filtration and weighing, we found this to correspond to a concentration of 0.17 mg/mL. We note that, even though the yield of the liquid phase exfoliation of MoO₃ is low (<0.1 %), the concentrations achieved are well in a range suitable for further processing (*e.g.* the formation of composites as demonstrated below). In fact, they are comparable to maximum concentrations in the case of early work on graphene exfoliation.¹⁷ Furthermore, the non-exfoliated material is not lost, as it can be subjected to further sonication based exfoliation runs to recycle the sediment.

Size selection of nanosheets

This optimised procedure yielded exfoliated nanosheets with typical lateral dimensions of 100 nm × 40 nm. We denote this material small-MoO₃ or s-MoO₃ and will characterise it below in detail. However, as shown in figure 1G, even smaller flakes can be obtained by centrifugation at higher rates. We have prepared very small nanosheets by centrifugation at 5000 rpm (~2600g) which we will also characterise in detail. These we denote very small-MoO₃ or vs-MoO₃. Alternatively, larger flakes can be prepared by a controlled centrifugation procedure.^{70, 78} The size-selection procedure for larger flakes involves a short initial centrifugation at low rpm to first remove unexfoliated powder in the sediment. The supernatant is then subjected to a second longer (or faster) centrifugation step to precipitate exfoliated material of larger sizes (while keeping the smaller exfoliated flakes – s-MoO₃ - in the supernatant). The sediment can then be redispersed in fresh solvent yielding a dispersion of larger flakes (l-MoO₃). This material will also be studied in detail.

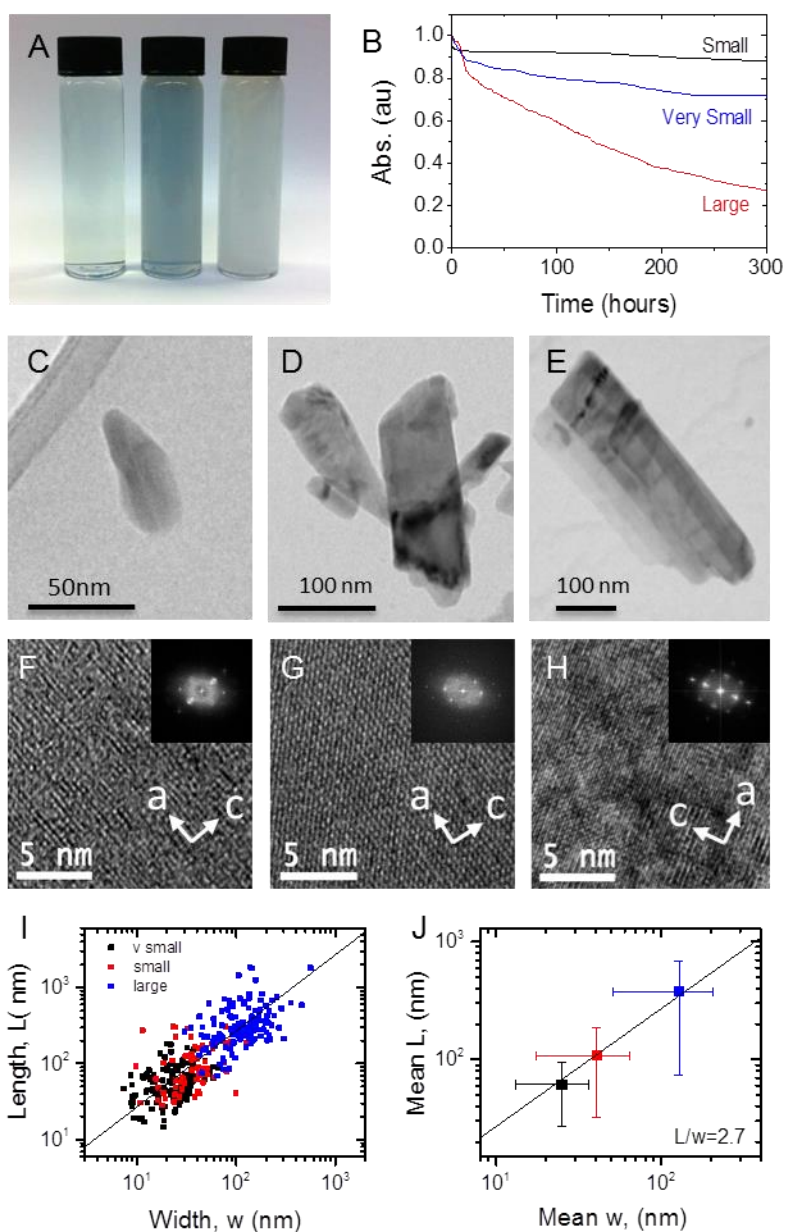


Figure 2: A) Dispersions of (left to right) very small (vs), small (s) and large (l) MoO_3 nanosheets in isopropanol. B) Sedimentation behaviour of dispersions of very small, small and large MoO_3 nanosheets. C-E) TEM and F-H) HRTEM images of typical very small, small and large MoO_3 nanosheets. The crystallographic directions are indicated on the panels. I) Nanosheet length plotted *versus* width for very small, small and large MoO_3 nanosheets determined from TEM. J) Mean length plotted *versus* mean width. The error bars represent standard deviations. The mean flake aspect ratio was $L/w=2.7$. In all cases dispersions were prepared using isopropanol and $C_i = 300 \text{ mg/mL}$, $t_s=5 \text{ hrs}$, $f = 1.5 \text{ krpm}$, $t_{CF} = 2 \text{ hrs}$.

Shown in figure 2A is a photograph of dispersions of vs-MoO₃, s-MoO₃ and l-MoO₃ in IPA. These dispersions are visually different: while the large nanosheet dispersion resembled a colour similar to that of the initial white powder, the smaller nanosheets yielded a faint blue colour in dispersion. Because the preparation procedure was designed to remove all unstable material, we expect the s-MoO₃ and therefore also the vs-MoO₃ dispersions to be stable. However, we expect the dispersions of l-MoO₃ to be less stable because they were produced by centrifugation of the nanomaterial at only 1,000 rpm (~100g). To test this, we performed sedimentation analysis, measuring the dispersion absorbance as a function of time over 300 h in a purpose built sedimentation apparatus.⁷¹ The data presented in figure 2B shows s-MoO₃ to be relatively stable with only 8% of the dispersed material sedimenting over this time. Surprisingly, the vs-MoO₃ was slightly less stable with ~20% fallout over 300 hrs. Conversely, the l-MoO₃ was unstable with ~75% sedimentation over 300 hrs. However, sedimentation is slow enough in all cases to allow further processing, for example to make films.

TEM analysis

TEM analysis was performed on vs-MoO₃, s-MoO₃ and l-MoO₃ by depositing a few drops of each dispersion onto TEM grids. In all cases, large numbers of quasi-2D objects were seen with typical examples shown on figures 2 C-E. We also performed high-resolution TEM (HRTEM) imaging, as shown in figure 2 F-H. These images clearly reveal the MoO₃ crystal lattice, evidencing the exfoliated material to be of high structural quality. Analysing each FFT (Fast Fourier Transform) confirmed the structure to be consistent with the layered alpha phase of MoO₃.⁷⁹⁻⁸¹ In addition, the lattice orientation could be determined: the viewing direction is roughly along the b-direction (*i.e.* the direction perpendicular to the nanosheets) while the a- and c-directions are noted in the images. We note that MoO₃ is unstable under the electron beam. This can be observed in both image and the FFT through the broadening and doubling of the peaks in the c-direction, as can be seen in figure 2F and 2H. As a result, it is important to avoid over-exposure to the electron beam, as this may result in a reduction of the MoO₃ through Magneli phases to MoO₂.⁴⁶

From the low resolution TEM images, we measured the length, L, and width, w, of ~100 nanosheets per sample. This data is plotted in figure 2I and clearly shows the length to scale approximately linearly with the width, suggesting a well-defined L/w ratio. In addition,

it confirmed that the lateral sizes scale as expected with $vs\text{-MoO}_3 < s\text{-MoO}_3 < l\text{-MoO}_3$. From this data we calculate the mean lengths and widths which are plotted in figure 2J. The mean nanosheet lengths were 61 nm, 108 nm and 378 nm for $vs\text{-MoO}_3$, $s\text{-MoO}_3$ and $l\text{-MoO}_3$, respectively. The mean width was perfectly proportional to the mean length giving a mean L/w ratio of 2.7, independent on nanosheet size. This well-defined L/w ratio can be attributed to the structure of individual MoO_3 monolayers.^{47, 49} These consist of two strata of MoO_6 octahedra stacked vertically in the b-direction to form a 2D monolayer. Bonding in the plane of each monolayer is through edge sharing oxygen bonds in the a- and c-directions while inter-strata bonding is through an axial oxygen bond in the b-direction. The octahedral bilayers contain three types of crystallographically inequivalent oxygen sites namely singly (in b-direction), doubly (in a-direction) and tertiary coordinated oxygen atoms (in c-direction).^{47, 49} That these sites are inequivalent is reflected in varying Mo-O bond lengths throughout each octahedral layer, ranging from 1.67 Å to 2.33 Å. We thus expect sonication-induced scission to result in a breakage of in-plane Mo-O bonds with the longest, weakest bond of the tertiary coordinated oxygen in c-direction being cleaved preferentially over the other Mo-O bonds. This yields nanosheets which are shorter in the c-direction relative to the a-direction and so have a well-defined aspect ratio.

AFM analysis

One of the advantages of using IPA as a solvent is that, due to its high volatility, it greatly facilitates deposition of nanosheets on surfaces, allowing the study of flake size and thickness by atomic force microscopy (AFM). This has the advantage over TEM in that it can give information about flake thickness, t , as well as length and width. However, because nanosheet aggregation can occur during deposition, it is important to ensure that flake size statistics are not strongly influenced by aggregation effects. Thus, only nanosheets that were clearly not reaggregated on the substrate were included in the statistical analysis of length, width and thickness. Shown in figure 3A are examples of an aggregated (left) and unaggregated (right) flake.

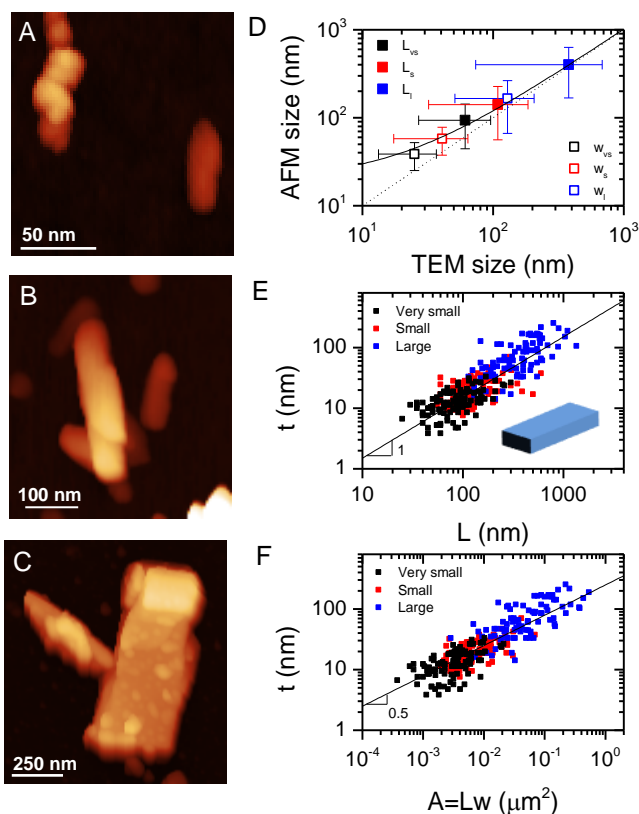


Figure 3: A, B, C) Representative AFM height images of vs-MoO₃, s-MoO₃ and l-MoO₃ respectively. D) Comparison of length, L , and width, w , of the dispersions determined by AFM and TEM. The dotted line illustrates the expected behaviour assuming AFM and TEM give the same lateral dimensions. The solid line illustrates the behaviour when AFM gives a value 20 nm larger than TEM. E) Flake thickness, t , determined by AFM analysis as a function of flake length, L . The line represents linearity. The inset cartoon illustrates the shape of an average flake. F) Nanosheet height plotted as a function of approximate nanosheets area (plotted as $L \times w$). The line represents square root behaviour.

For each sample type we imaged large numbers of flakes (figure 3A-C) and measured L , w and t for ~ 100 unaggregated flakes. First, we plotted the mean lateral size (*i.e.* $\langle L \rangle$ or $\langle w \rangle$) against the equivalent value measured by TEM (figure 3D). We found the agreement to be almost perfect (perfect agreement indicated by dotted line). However, fitting showed the AFM sizes to be ~ 20 nm larger than those from TEM (solid line). This is consistent with broadening due to tip-convolution effects. In any case, this implies the AFM data to be free of

aggregation effects (or at least that the TEM and AFM samples suffer the same degree of aggregation).

Given that the TEM data revealed that $\langle L \rangle \propto \langle w \rangle$, we focus on the L and t data. Plotted in figure 3E is a graph of nanosheet thickness *versus* length. There are a number of significant pieces of information in this graph. First the nanosheets' thicknesses scale as $vs\text{-MoO}_3 < s\text{-MoO}_3 < l\text{-MoO}_3$ with mean thicknesses of 14 nm, 21 nm and 80 nm respectively. For the $vs\text{-MoO}_3$, the thinnest nanosheets have $t \sim 3\text{-}4$ nm, consistent with only a few stacked MoO_3 monolayers (for $s\text{-MoO}_3$ and $l\text{-MoO}_3$, the thinnest flakes are 7.5 and 14 nm respectively). In addition, the thickness scales in proportion to the length for all measured nanosheets suggesting the presence of a well-defined L/t ratio with a mean value of 6.6. This means that, on average MoO_3 nanosheets have dimensions that scale as $L:w:t=6.6:2.5:1$. This shape is illustrated by the inset cartoon in figure 3H and shows these objects to be closer in shape to nano-bricks than nanosheets.

However, the proportionality of length and thickness is probably not a fundamental relationship. It is more likely that the thickness is related directly to the nanosheet area and so indirectly to the length (and width). The energy required to exfoliate a MoO_3 crystallite is expected to scale linearly with the crystallite area. Thus, for a given amount of energy available, we expect a large-area crystallite to be exfoliated to give fewer, thicker nanosheets compared to a small area crystallite which should give more, thinner nanosheets. Thus, we expect the flake thickness to depend on the area as a monotonically increasing function. To explore this, we plot the flake thickness *versus* the approximate flake area, A, (estimated from $A=Lw$, figure 3F). We find a well-defined relationship, consistent with $t \propto \sqrt{A}$. As $A=Lw$ and $L \propto w$, this is of course consistent with $t \propto L$.

With these AFM results in mind, we can consider the possibility of obtaining monolayer MoO_3 by liquid exfoliation. The data in figure 3E suggests that when exfoliation is performed in IPA, nanosheets with lateral size of ~ 8 nm should be monolayer. It may be possible to produce such small nanosheets by sonication induced scission and/or size selection.^{24, 78, 82} In addition, such objects would be 2-dimensional quantum dots with potentially interesting optical properties. In this work we focused on the solvent IPA to facilitate the AFM analysis. However, other solvents, particularly those with solubility parameters closer to $20.7 \text{ MPa}^{1/2}$, may result in more complete exfoliation (although

deposition on substrates may be challenging if, as is often the case, such solvents have high boiling points). Thus, a more complete solvent-dependent study could lead to dispersions with reasonable monomer contents.

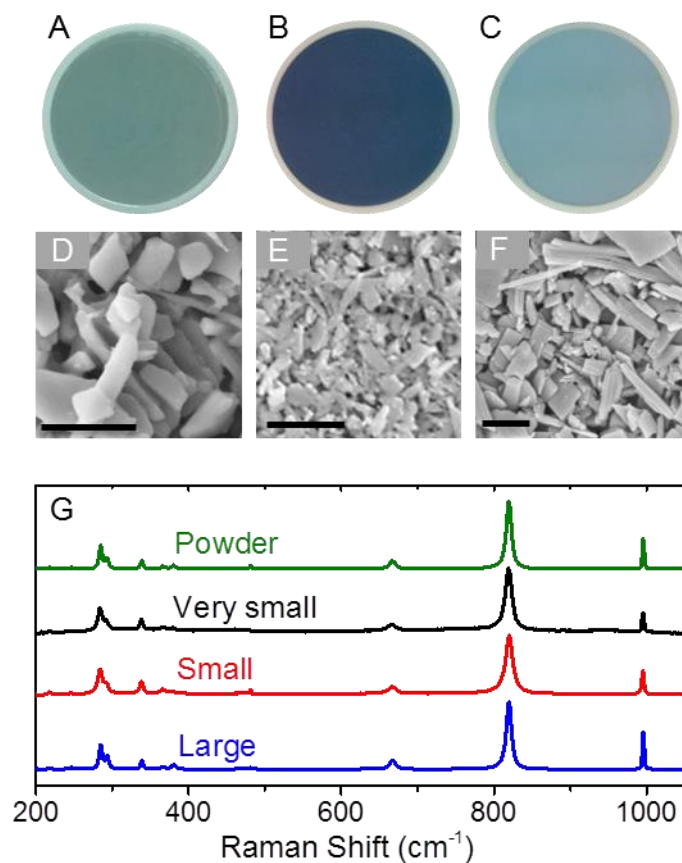


Figure 4: A-C) Optical and D-F) SEM images of vacuum filtered films of vs-MoO₃, s-MoO₃ and l-MoO₃ respectively (scale bar 500 nm). G) Raman spectra of bulk MoO₃ powder and films of vs-MoO₃, s-MoO₃ and l-MoO₃.

Formation and Characterization of Films

To gain further insights in the structural properties of our material, the dispersions were filtered onto alumina membranes to form films which were characterised using scanning electron microscopy (SEM) and Raman spectroscopy. Shown in figure 4A-C are photographs of filtered films of vs-MoO₃, s-MoO₃ and l-MoO₃ respectively. The colour difference observed in the dispersions is clearly evident in the filtered material. We analysed the surface of all three film types with SEM (figure 4 D-F). While the films are homogenous over long length-scales, they consist of disordered arrays of nanosheets over short length-scales.

Thin films such as those in figure 4A-C are ideal for characterisation by a number of spectroscopic techniques. Shown in figure 4G are Raman spectra ($\lambda_{\text{ex}}=532$ nm) of filtered films of vs-MoO₃, s-MoO₃ and l-MoO₃ nanosheets in comparison to the starting powder. It has long been known that the Raman spectrum of MoO₃ is particularly rich in information, providing insight into phase, crystallite size, content of oxygen vacancies and stoichiometry of the material.⁸³ All four spectra in figure 4G display the characteristic peaks expected for orthorhombic alpha-phase MoO₃.^{84, 85} According to Dieterle et al., the ratio of the intensities of the 285 cm⁻¹ peak to that at 295 cm⁻¹ provides a measure of the true stoichiometry of the material.⁸³ Performing this analysis, the raw powder yields a stoichiometry of MoO_{2.96}, while the processed very small, small and large nanosheets have a slightly lower stoichiometry of MoO_{2.94}, MoO_{2.95}, MoO_{2.95}, respectively. We attribute this slight alteration of the stoichiometry to the reduced size of the nanosheets compared to the powder. It is believed that defects, such as oxygen vacancies, accumulate at edge regions resulting in a disruption of the bonding arrangement.^{86, 87} Nevertheless, the stoichiometry change is a minor one implying that solution processing introduces very few defects into the exfoliated material, as further corroborated by the absence of side-bands around the M=O stretching vibration at 996 cm⁻¹ which would be characteristic for the presence of oxygen vacancies. The fact that sonication does not introduce defects is perhaps not surprising. It is well known that sonication-assisted exfoliation of graphite to give graphene does not introduce significant quantities of basal plane defects.^{17, 24}

Photoluminescence

The analysis of nanosheet size given above suggests that all but the smallest nanosheets are actually thick enough to be considered bulk-like. However, it is possible that the exfoliation process involves a comprehensive exfoliation step followed by a degree of reaggregation in solution. In this case, the observed nanosheets may in fact be restacked objects with inter-layer coupling that is considerably weaker than for bulk crystallites. This weak coupling may be caused by trapped inter-layer solvent, resulting in electronic properties significantly different to bulk MoO₃. In order to probe whether the degree of exfoliation influences the electronic structure of the MoO₃, we have performed photoluminescence (PL) measurements of both dispersions and dried filtrates prepared from them. As the photoluminescent response is sensitive to the electronic structure of the material, we expect photoluminescence to reveal any electronic structural differences between exfoliated

nanosheets and bulk MoO₃. Bulk MoO₃ is a wide band gap semiconductor (band gap >3 eV) exhibiting reasonable fluorescence.^{80, 88, 89} It has been previously demonstrated that oxygen vacancies, impurities and defects create additional states between the valence and conduction band resulting in a reduction of the optical band gap yielding typical fluorescence features centered around 400-450 nm (2.75-3.1 eV).^{80, 88, 90-94} Accordingly, it has been suggested that photoluminescence on MoO_x (where $x \approx 3$) films provides a valuable handle to probe crystallinity, stoichiometry and even surface roughness of the samples.⁹¹ However, the broad near-band edge emission at < 400 nm usually obscures the lower energy features which are characteristic of sample quality.

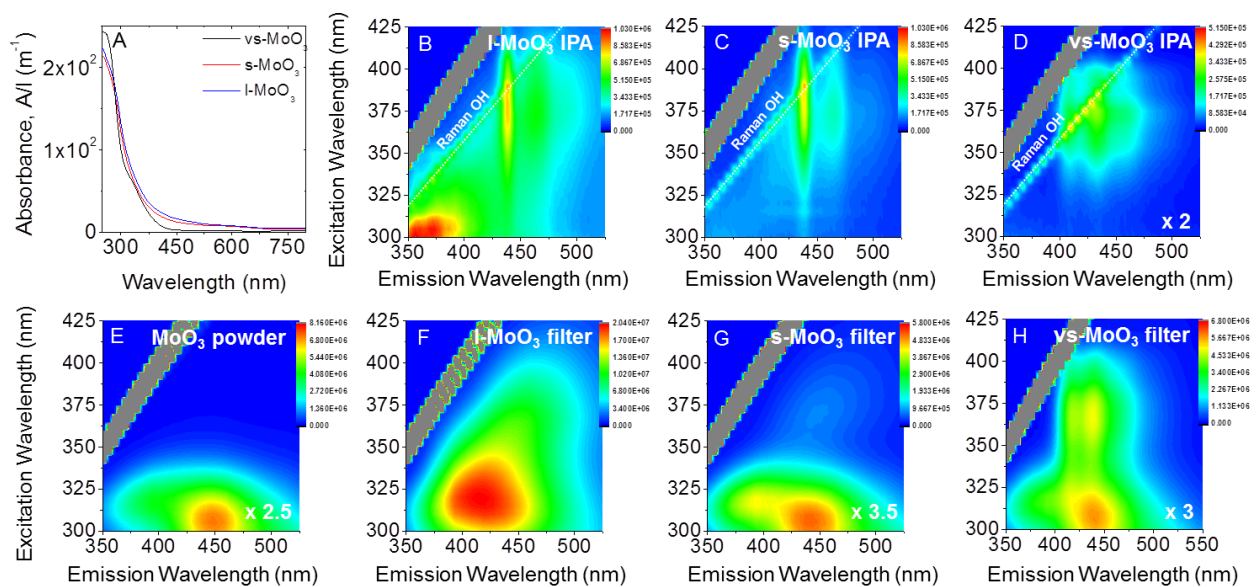


Figure 5: A) Absorbance spectra of vs-MoO₃, s-MoO₃ and l-MoO₃ dispersions (diluted to similar optical densities) used for studying fluorescence. B-D) Photoluminescence excitation-emission contour plots of l-MoO₃, s-MoO₃ and vs-MoO₃ dispersions in IPA, respectively. E-H) Photoluminescence excitation-emission contour plots of E) MoO₃ starting powder, and F-H) filtered dispersions of l-MoO₃, s-MoO₃ and vs-MoO₃, respectively.

To characterize the photoluminescence, we prepared dispersions of vs-MoO₃, s-MoO₃, l-MoO₃ with the similar absorbance as shown in figure 5A. For each dispersion, we measured excitation-emission photoluminescence maps (figure 5 B-D). These can be compared with a PL map for the starting powder (figure 5E). The starting powder displays the typical broad fluorescence centered at 450 nm when excited in the UV region. As shown

in figure 5 B-D, new very sharp photoluminescence features are found in all MoO₃ dispersions. The main emission feature is still centered in the same region (430 nm), but evolves when exciting at lower energies (375 nm opposed to 310 nm) and is significantly sharper, showing a well resolved fine-structure. This implies the electronic decoupling of the layers in the exfoliated state in the liquid. We would like to emphasize that this is in marked contrast to previous observations on MoO₃ nanorods colloiddally dispersed in ethanol: in this system, the weak PL observed in the dried powder was absent in the solvent system.⁹⁴ In the case of the vs-MoO₃ dispersion, the PL intensity is reduced by approximately a factor of 2 compared to s-MoO₃ and l-MoO₃ and an additional feature evolves at lower wavelength, possibly pointing to an alteration of the electronic properties due to edge effects.

The Raman spectra presented in figure 4 G make irreversible changes in the MoO₃ structure associated with the processing procedure unlikely. However, to categorically rule out the possibility that these new PL features represent such changes, we filtered the dispersions described above through porous membranes to give films (see below for details). We measured PL maps for each of these films (figure 5 F-H). These maps are dominated by broad features associated with low excitation wavelengths which are very similar to the features observed in the MoO₃ starting powder. This implies that during film formation, extensive reaggregation occurs with the flakes re-stacking to create an electronic environment very similar to that found in the powder. This may be associated with near complete solvent removal, allowing the re-establishment of strong inter-layer coupling. These results largely rule out the possibility of irreversible changes to MoO₃ structure on exfoliation (as already suggested by the Raman data). However, for each of the filtered films, the maps contain weak features analogous to those observed in the dispersions. This implies that not all of the nanosheets restack perfectly upon filtration.

This data clearly shows that the photoluminescence is highly sensitive to the exfoliation state of the nanomaterial. This suggests the degree of exfoliation to be more complete than that concluded from the exfoliated nanosheets' thicknesses and may mean the nanosheets consist of multiple restacked sub-units, perhaps separated by residual solvent. Furthermore, this implies that the photoluminescence can be in turn used to assess the exfoliation state of the material.

Applications as supercapacitor electrodes

One of the most important advantages of liquid exfoliation is that it facilitates solution processing, leading to the facile production of structures that would otherwise be time-consuming or even impossible to prepare. For example, the production of thin films from solution-processed nanosheets is much faster and easier than would be the case using other methods.¹⁶ More importantly, liquid exfoliation allows the production of more complex arrangements such as polymer/nanosheet or nano-material/nanosheet composites. Examples of the latter material type are mixtures of different types of 2D materials or combinations of 2D materials with 1D nano-structures such as nanotubes.^{16, 42, 95} These composites have been shown to be useful in applications such as battery electrodes⁴² and thermo-electrics.^{16, 35}

In the following section, we demonstrate the advantages of liquid exfoliation of MoO₃ by using this technique to prepare high-performance supercapacitors. A number of studies have shown that MoO₃ nanostructures have potential for use as electrodes in supercapacitors⁵⁰⁻⁵² as well as Li ion battery applications.⁵³⁻⁵⁷ In fact solution-exfoliated MoO₃ nanosheets may be particularly promising in this area. Firstly, solution-prepared nano-materials have distinct advantages in terms of ease of processing, for example facilitating film formation by a variety of methods such as spray deposition.^{96, 97} In addition, 2D materials have large specific surface areas which may lead to large capacitances.⁹⁸ Moreover, even if not fully exfoliated there is scope for intercalation of charge between the layers further enhancing the capacitance (at least at low rates). Finally, by analogy with films of graphene nanosheets,²⁴ we expect MoO₃ films, such as those shown in figure 4 D-F, to have reasonable porosities allowing electrolyte infusion and access of ions to the internal surface.

Owing to the solubility of MoO₃ in aqueous media,^{99, 100} the charge storage properties of MoO₃ nanosheets were investigated in an organic based electrolyte (1 M LiClO₄ in propylene carbonate). This was performed in a half-cell configuration using Li sheets as reference and counter electrodes. Electrodes of solely vs-MoO₃, s-MoO₃ and l-MoO₃ achieved low charge storage of ~2 F/g (dV/dt=10 mV/s) as shown by cyclic voltammograms (CVs) in Figure 6A. The low charge storage was attributed to limitations in electrical conductivity ($\sigma \sim 10^{-6}$ S/m, 1 μ m thickness) of MoO₃.^{49, 101} This limits the rate at which electrons can be transported between active sites for charge storage and current collectors. A number of papers have shown that such limitations can be addressed by introducing nanostructured conductive networks into the electrode material.^{35, 42, 102-107} Here, we pursue such a strategy by preparing composite electrodes by blending the MoO₃ nanosheets with

single walled carbon nanotubes (SWNTs). A set of mixed dispersions of SWNTs and MoO₃ were prepared and formed into composite thin films for testing as supercapacitor electrodes. Such composites are known to retain properties of the 2D matrix yet display conductivities which can be varied over 9 orders of magnitude.^{16, 35, 95} Previously, similar systems have been used to improve the properties of MoS₂-based Li-ion battery electrodes⁴² and TMD-based thermoelectric materials.^{16, 35}

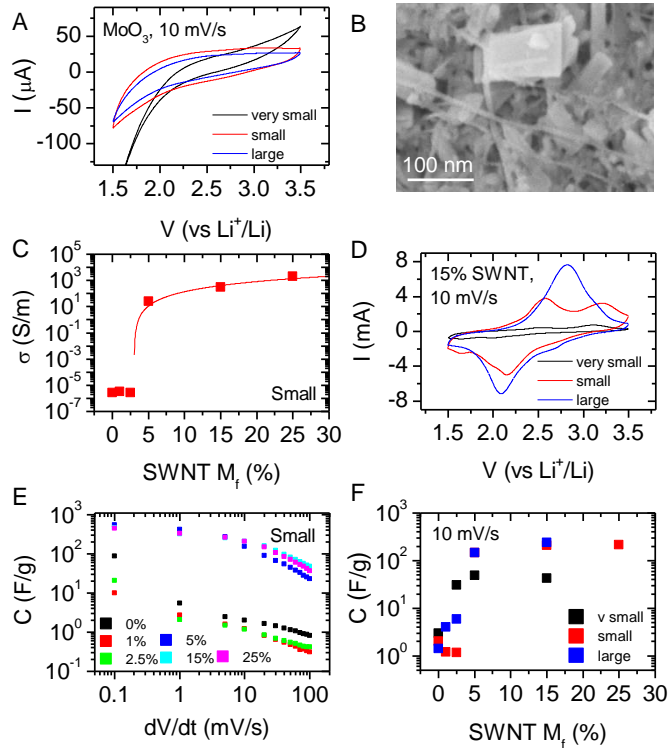


Figure 6: Characterisation of MoO₃ films as electrodes in supercapacitors (Electrode area = 2.54 cm²). A) Cyclic voltammograms at 10 mV/s for electrodes prepared from vs-MoO₃, s-MoO₃ and l-MoO₃ using a three electrode cell. (Film thickness = 1 µm as determined by profilometry, Electrolyte = 1 M LiClO₄ in propylene carbonate.) B) SEM image of a MoO₃/SWNT composite film (M_f = 25%). C) Electrical conductivity of thin films (~1 µm thick) of s-MoO₃:SWNT composites plotted as a function of nanotube mass fraction. D) Cyclic voltammograms for composite electrodes prepared from matrices of vs-MoO₃, s-MoO₃ and l-MoO₃ filled with 15wt% SWNTs (dV/dt = 10 mV/s). E) Gravimetric capacitance plotted as a function of scan rate for electrodes of MoO₃ and MoO₃/SWNT composites with a range of nanotube mass fractions. F) Gravimetric capacitance plotted as a function of SWNT mass fraction for composites based on vs-MoO₃, s-MoO₃ and l-MoO₃ (dV/dt = 10 mV/s).

Shown in figure 6B is an SEM image of the surface of such a composite (25wt% SWNTs). This clearly shows excellent mixing of SWNTs and MoO₃ nanosheets which should facilitate charge transport throughout the electrode. In addition, the electrodes have a degree of mesoporosity which is required to allow access of electrolyte to the internal surface of the MoO₃.⁹⁷

We measured the electrical conductivity of such composites as a function of SWNT mass fraction, M_f (figure 6C). The conductivity remained unchanged until a nanotube content of ~3 wt% where it underwent a sharp increase, reaching ~1000 S/m for 25wt% nanotubes. This behaviour is consistent with percolation theory; the sharp increase is associated with the formation of the first conducting paths of networked nanotubes which extend through the film.¹⁰⁸ Such percolation effects have been observed for a range of systems including graphene/MoS₂ and SWNT/MoS₂ composites.⁹⁵ The conductor loading level where the first conducting path occurs is known as the percolation threshold, $M_{f,c}$. Above this, the conductivity scales approximately as

$$\sigma \propto (M_f - M_{f,c})^t \quad (3)$$

where t is the percolation exponent. Strictly speaking, this expression should be written in terms of volume fraction rather than mass fraction.¹⁰⁸ However, this approximation works reasonably well up to ~30 wt%. The percolation exponent is often observed to be close to 2.0,¹⁰⁹ the so-called universal value.¹⁰⁸ Setting $t=2.0$, the solid line in figure 6B shows the data to be consistent with percolation theory with $M_{f,c}=3$ wt%. This value is very similar to that found for SWNT/MoS₂ composites.⁹⁵

Composite electrodes of vs-MoO₃, s-MoO₃ and l-MoO₃ mixed with SWNTs were prepared and their charge storage properties investigated for a range of SWNT contents (1-25 wt%). Figure 6D shows CVs measured for 15 wt% composites prepared with vs-MoO₃, s-MoO₃, and l-MoO₃ (dV/dt=10 mV/s). For each sample, the capacitance per unit mass of the electrode associated was ~200 F/g, representing a 100-fold increase relative to the capacitance of a MoO₃-only electrode.

These results warrant a more detailed investigation into the properties of MoO₃/SWNT supercapacitors. We measured CVs at a range of scan rates for composite supercapacitor electrodes prepared from all three MoO₃ types with nanotube contents from 0-

25 wt%. Figure 6E shows the measured gravimetric capacitance plotted *versus* scan rate for s-MoO₃. Electrodes with a SWNT content below 3 wt% had small capacitance that fell from ~20 F/g at 0.1 mV/s to <1 F/g at 100 mV/s. However, for nanotube contents above the percolation threshold ($M_{f,c}=3$ wt%), much larger capacitances were observed, with similar values found for the 5, 15 and 25 wt% samples. Values as large as 540 F/g were found at scan rates of 0.1 mV/s. While the capacitance fell with increasing scan rate, values as high as 20-40 F/g were observed at scan rates of 100 mV/s.

The mechanisms contributing to charge storage in these systems are expected to be ion intercalation, redox pseudocapacitance and double layer capacitance.⁵² Interlayer ion intercalation in MoO₃ is limited by its characteristic slow kinetics⁵² and is probably only significant for $dV/dt < 0.1$ mV/s. At intermediate scan rates, capacitances of ~200 F/g are probably dominated by pseudocapacitive effects similar to those observed in iron oxides and manganese oxides.¹¹⁰⁻¹¹³ At higher rates, the capacitance is probably limited by diffusion of ions into the pores of the electrode.

We can summarise the supercapacitor data by plotting the capacitance ($dV/dt=10$ mV/s) as a function of SWNT content in figure 6F. For each of the MoO₃ types, the behaviour is roughly the same. For low nanotube contents, below the percolation threshold (~3 wt%), the capacitance is relatively low (1-6 F/g). However, between 2.5 and 5 wt%, the capacitance increases sharply, saturating at ~200 F/g for mass fractions greater than 5 wt%. We note that this sharp increase occurs exactly at the percolation threshold implied by the data in figure 6C. This clearly shows that the sharp increase in capacitance is related to the onset of electrical conductivity which occurs as the first conducting paths through the films are formed.

We note that this increase cannot be attributed to contributions from the capacitance of the SWNTs themselves. We measured the capacitance of a SWNT-only film finding ~2 F/g (10 mV/s), very close to the MoO₃ value. If the capacitance was just the weighted mean of MoO₃ and SWNT contributions, it would remain constant at ~2 F/g for all SWNT contents. This is clearly not what is observed. Rather, the increase in capacitance is due to the presence of the nanotubes which facilitate charge transport from the MoO₃/electrolyte interface to the external circuit. This means that the maximised values of capacitance observed in figures 6E and F can be associated with the intrinsic capacitance of MoO₃ itself

(in this electrode arrangement). The capacitance achieved is comparable to that previously reported for MoO₃ electrodes: 349 F/g for α -MoO₃ nanobelts (CV, 0.1 mV/s),⁹⁷ 303 F/g for mesoporous α -MoO₃ (CV, 1 mV/s),⁵² 405 F/g for α -MoO₃ microrods (galvanostatic charge-discharge at 50 mA/g, 2 to 3.5 V).⁵⁵

Percolation-based phenomena are highly non-linear. For example a small change in nanotube content can result in an extremely large change in conductivity as shown in figure 6C. This also clearly applies to capacitance which displays a rapid increase around 3 wt%. Because of this, it will be possible to engineer composite supercapacitor electrodes with extremely large capacitance changes on the addition of very small amounts of nanotubes. Indeed, the percolation threshold associated with composites filled with 1-dimensional nano-conductors is known to scale with the ratio of conductor diameter to length.¹¹⁴ Thus, by using extremely long, yet narrow SWNTs, the percolation threshold could be suppressed to occur well below 1 wt%. Indeed this behaviour is not limited to MoO₃-based systems. SWNTs (or graphene) can be used to dramatically improve the capacitance of a range of low conductivity, solution-processable nano-materials such as manganese or nickel oxide.^{103, 107} By tuning the percolation behaviour, significant performance increases will be achieved at very low nano-conductor content.

CONCLUSIONS

In conclusion, we have demonstrated liquid exfoliation of molybdenum trioxide powder to give MoO₃ nanosheets. This can be achieved by sonicating the powder in a range of solvents characterized by Hildebrand solubility parameters close to 21 MPa^{1/2}. The concentration of dispersed solvent is described very well by classical solution thermodynamics. While the size of the exfoliated nanosheets can be tuned by controlled centrifugation, only nanosheets below 200-300 nm in length remain stably dispersed over long periods. The length, width and thickness of the nanosheets were correlated such that L:w:t=6.6:2.5:1. We attribute this to the bonding regime within the nanosheets coupled with the scaling of exfoliation energy required with flake area. The thinnest flakes are only a few monolayers thick. However, photoluminescence spectroscopy suggests much thicker nanosheets to have electronic properties that differ from the bulk, while Raman spectroscopy indicates that the exfoliation process does not induce defect formation. One of the advantages of liquid exfoliation is that it facilitates the formation of films and composites. We prepared

films of MoO₃ nanosheets for use as supercapacitor electrodes. These displayed capacitances of ~2 F/g at 10 mV/s. However, addition of >3 wt% nanotubes resulted in composite electrodes with capacitances of ~200 F/g at 10 mV/s and as high as ~500 F/g at 0.1 mV/s.

This work clearly underlines that solvent exfoliation can be applied to materials beyond the accepted group comprising graphene, BN and transition metal dichalcogenides. We believe this is the first step toward the demonstration of the generality of this exfoliation concept. By following similar protocols, we envisage exfoliation of a wide range of van der Waals bonded layered materials from other layered oxides and III-VI materials (GaS, InTe etc) to more exotic materials such as layered metal halides and beyond. This will allow us to study the physical and chemical properties of a vast range of new 2D materials and may facilitate a range of previously inaccessible applications. We are convinced that this approach will inspire the development of advanced applications of 2D layered materials.

METHODS

Materials

Molybdenum trioxide powder (99.98%, CAS 1313-27-5) and all solvents used were purchased from Sigma Aldrich at the highest available purity. P3 SWNT's were purchased from Carbon Solutions. All reagents were used as received.

Dispersion of MoO₃ nanosheets

Initial solvent screening: 1 mg/mL MoO₃ was sonicated in 10 mL of the respective solvent for 15 min at 25 % amplitude with a horn probe sonic tip (VibraCell CVX, 750W, 25% amplitude) while ice-cooling the dispersion. The resulting dispersion was centrifuged for 50 min at 1,500 rpm (~240 g) in a Hettich Mikro 220R centrifuge. The supernatant was decanted and subjected to absorbance spectroscopy.

The centrifugation parameters used in the solvent screening were established by a methodology to minimise the effects of solvent viscosity. The most viscous solvent in our screening study was *N*-Cyclohexyl-2-pyrrolidone (CHP, $\eta=11.5$ mPa.s), therefore CHP will require the longest centrifugation time (at a given rate) for the nanosheets to reach a steady state concentration. Preliminary experiments investigating the dependence of CHP-dispersed MoO₃ concentration on centrifugation time, t_{CF} , established that, when centrifuging at $f=1.5$

krpm ($\sim 240g$), steady state was achieved after $t_{CF} = 50$ mins. Because particles sediment faster in a lower viscosity solvent, applying these parameters to the other (lower viscosity) solvents ensures a steady state concentration. The following solvents were used for the screening: CHP, *N,N'*-dimethyl-*N,N'*-trimethyleneurea (DMPU), cyclohexanone, 2-propanol (IPA), *N*-methyl-2-pyrrolidone (NMP), *N,N*-dimethylformamide (DMF), tetrahydrofuran (THF), chloroform, toluene, heptane, pentane and methanol.

Preparation of MoO₃ stock dispersion: Molybdenum trioxide powder (30 g) was added to 2-propanol (100 mL) in a 140 mL open top, flat bottomed beaker. The beaker was connected to an external cooling system that allowed for cooled water (5⁰C) to flow around the dispersion during sonication. The dispersion was sonicated using a horn probe sonic tip (VibraCell CVX, 750W, 25% amplitude) for 5 h unless otherwise noted. The sonic tip was pulsed for 9s on and 2 s off to avoid damage to the processor and reduce any solvent heating.

Optimisation of dispersion parameters: Centrifugation parameters were optimised using the above dispersion procedure with an initial concentration of 50 mg/mL. Aliquots of 25 mL were centrifuged in a Hettich Mikro 220R centrifuge in 28 mL vials for varying time periods (10 mins to 250 mins) and rotation rates (f ; 500-2,000 rpm, 26 g-430 g). The top 20 mL were decanted from the vial and diluted to perform absorption spectroscopy using a Cary 6000i in a 1 cm optical grade quartz cuvette. The concentration study entailed varying the initial concentration of MoO₃ in 100 mL IPA and determining the resultant absorbance at 375 nm as a measure for the concentration after centrifuging aliquots of 25 mL (in 28 mL vials) for 110 min at 1,500 rpm ($\sim 240g$). The sonication time study experiments comprised an initial concentration of 300 mg/mL. During sonication (VibraCell CVX, 750W, 25% amplitude, pulse 9 s on, 2 s off) 5 mL aliquots were removed at given time periods and centrifuged 1,500 rpm ($\sim 240g$) for 110 mins in 10 mL vials. The supernatant was again decanted and analysed using absorption spectroscopy. We note that A/l from the sonication time study is not directly comparable to the values yielded by the other optimisation procedures due to the slightly altered centrifugation conditions (different liquid volumes).

Nanosheet size selection: vs-MoO₃- 25 mL aliquots of stock dispersion described above were centrifuged at 5 krpm (2600g) for 120 mins. The supernatant was subsequently decanted and characterised as vs-MoO₃. s-MoO₃- Aliquots of stock dispersion were centrifuged at 1.5 krpm ($\sim 240g$) for 110 mins ($3\tau_2$ as described in results and discussion section). The supernatant was

decanted from the vial and characterised as s-MoO₃. l-MoO₃- Aliquots of stock dispersion were centrifuged at 1 krpm (~100 g) for 30 mins ($3\tau_1$) to remove any large unexfoliated material. The supernatant was decanted from the vials and further centrifuged at 1 krpm for 105 mins ($>\tau_2$). The supernatant was decanted and discarded while the sediment was redispersed in fresh IPA.

Preparation of MoO₃/CNT composites

A MoO₃ dispersion was prepared as outlined above. P3 SWNT's (5 mg) were dispersed in IPA (50 mL) at a concentration of 0.1 mg/mL. This solution was then sonicated for 30 mins in a horn probe sonic tip (40% amplitude 750W processor), then sonicated for one hour in a sonic bath followed by an additional 30 min in the horn probe tip. This dispersion was then mixed directly (*i.e.* no centrifugation) with a predetermined concentration of MoO₃ dispersion to form a composite of known wt%. The concentration of MoO₃ dispersion was obtained from accurate weighing of an alumina membrane (pore size 25nm) before and after filtration.

Film formation, electrochemical and electrical measurements

Composite dispersions were filtered onto a nitrocellulose membrane and dried at room temperature. These films were subsequently transferred onto an aluminium electrode coated in an adhesive polymer (polyethylenimine (PEI)) using the transfer method of Wu et al.¹¹⁵ and the film thickness was determined by profilometry. The electrochemical electrode was cut out of this larger aluminium electrode using an 18 mm diameter punch. The sample electrode was then placed in an EL-cell in a half-cell configuration using a Li-ion based electrolyte (1 M LiClO₄ in propylene carbonate) in an atmosphere controlled glove box. Li foil was used for both counter and reference electrodes. Electrochemical testing was performed using a Reference 600 Gamry potentiostat. Capacitance was calculated from the cyclic voltammograms by integrating the current passed during the negative sweep, and dividing by the voltage range used (2V). The capacitance was normalised to the mass of the electrode material (MoO₃ + SWCNT, typically ~0.7 mg). Electrical conductivity was calculated using a four probe method with a Keithley 2400 source metre. Silver electrodes were used where the electrode spacing's were typically on the order of a millimetre.

Characterisation and Equipment

Optical absorbance was measured on a Varian Cary 5000 in quartz cuvettes with a pathlength of 1 cm. If necessary, the dispersions were diluted by pure solvent immediately prior to the measurement to yield optical densities below 1.5. Centrifugation was performed using a Hettich Mikro 220R centrifuge equipped with a fixed angle rotor 1060. We quote centrifugation rates both in terms of rpm and relative centrifugal force, RCF (relative to $g=9.8 \text{ ms}^{-2}$). For this centrifuge these parameters are related *via* $RCF = 106.4f^2$ where f is the rotation rate in krpm. Sedimentation measurements were conducted using a homemade device consisting of a series of lasers equi-positioned along the length of a quartz cuvette and photodiodes (650 nm).

Atomic force microscopy (AFM) was carried out on a Veeco Nanoscope-IIIa (Digital Instruments) system equipped with a E-head (13 μm scanner) in tapping mode after depositing a drop of the dispersion (10 μL) on a pre-heated (100 $^\circ\text{C}$) Si/SiO₂ wafer with an oxide layer of 300 nm. Typical image sizes were 2.5-5 μm at scan rates of 0.4-0.6 Hz. Bright field transmission electron microscopy imaging was performed using a JEOL 2100, operated at 200 kV while HRTEM was conducted on a FEI Titan TEM (300 kV). Holey carbon grids (400 mesh) were purchased from Agar Scientific and prepared by diluting dispersion to a low concentration and drop casting onto a grid placed on a filter membrane to wick away excess solvent. Statistical analysis (both AFM and TEM) was performed of the flake dimensions by measuring the longest axis of the nanosheet and assigning it “length” then measuring an axis perpendicular to this at its widest point and assigning it “width”.

Photoluminescence was acquired on a Fluorolog-3 spectrometer (Horiba Scientific) with a thermoelectrically cooled R928P photomultiplier tube detector. The samples were excited with a 450 W Xe lamp with a double monochromator in excitation (600 grooves/mm, 500 nm blaze grating). A slit width of 3 nm in both excitation and emission was used with a dwell time of 0.3 s. All spectra were corrected for the light intensity at a given wavelength recorded with a reference diode. Solid samples were measured in front phase in 45 $^\circ$ angle from the starting powder or filter papers, respectively. Dispersions were probed in right angle in 0.4x1cm quartz cuvettes after dilution to an optical density of 0.4 at 365 nm.

SEM analysis was performed using a Zeiss Ultra Plus. Raman spectroscopy was performed using a WITec alpha 300 with 532 nm excitation laser and a laser power of < 1

mW. In all cases spectra shown are an average from a line scan consisting of 25 individual measurements.

Acknowledgements: JNC acknowledges financial support from the ERC grant SEMANTICS and the SFI grant number 11/PI/1087. CB acknowledges the German Research Foundation DFG (BA 4856/1-1).

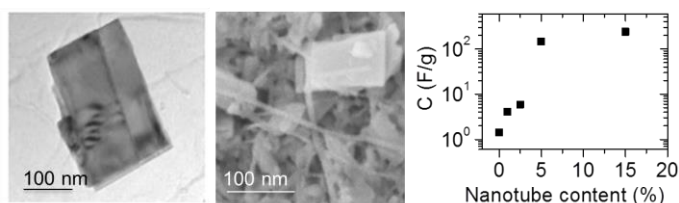
References

1. Novoselov, K. S.; Geim, A. K.; Morozov, S. V.; Jiang, D.; Zhang, Y.; Dubonos, S. V.; Grigorieva, I. V.; Firsov, A. A., *Science* **2004**, 306, 666-669.
2. Geim, A. K., *Science* **2009**, 324, 1530-1534.
3. Novoselov, K. S.; Fal'ko, V. I.; Colombo, L.; Gellert, P. R.; Schwab, M. G.; Kim, K., *Nature* **2012**, 490, 192-200.
4. Nicolosi, V.; Chhowalla, M.; Kanatzidis, M. G.; Strano, M. S.; Coleman, J. N., *Science* **2013**, 340, 1420-+.
5. Wilson, J. A.; Yoffe, A. D., *Advances in Physics* **1969**, 18, 193-&.
6. Wang, Q. H.; Kalantar-Zadeh, K.; Kis, A.; Coleman, J. N.; Strano, M. S., *Nature Nanotechnology* **2012**, 7, 699-712.
7. Chhowalla, M.; Shin, H. S.; Eda, G.; Li, L. J.; Loh, K. P.; Zhang, H., *Nature Chemistry* **2013**, 5, 263-275.
8. Osada, M.; Sasaki, T., *Advanced Materials* **2012**, 24, 210-228.
9. Osada, M.; Sasaki, T., *Journal of Materials Chemistry* **2009**, 19, 2503-2511.
10. Velde, B., *Introduction to clay minerals: chemistry, origins, uses, and environmental significance*. Chapman & Hall: 1992.
11. Frindt, R. F., *Journal of Applied Physics* **1966**, 37, 1928-&.
12. Novoselov, K. S.; Jiang, D.; Schedin, F.; Booth, T. J.; Khotkevich, V. V.; Morozov, S. V.; Geim, A. K., *Proceedings of the National Academy of Sciences of the United States of America* **2005**, 102, 10451-10453.
13. Zhan, Y. J.; Liu, Z.; Najmaei, S.; Ajayan, P. M.; Lou, J., *Small* **2012**, 8, 966-971.
14. Reina, A.; Jia, X. T.; Ho, J.; Nezich, D.; Son, H. B.; Bulovic, V.; Dresselhaus, M. S.; Kong, J., *Nano Letters* **2009**, 9, 30-35.
15. Coleman, J. N., *Accounts of Chemical Research* **2013**, 46, 14-22.
16. Coleman, J. N.; Lotya, M.; O'Neill, A.; Bergin, S. D.; King, P. J.; Khan, U.; Young, K.; Gaucher, A.; De, S.; Smith, R. J.; Shvets, I. V.; Arora, S. K.; Stanton, G.; Kim, H.-Y.; Lee, K.; Kim, G. T.; Duesberg, G. S.; Hallam, T.; Boland, J. J.; Wang, J. J.; Donegan, J. F.; Grunlan, J. C.; Moriarty, G.; Shmeliov, A.; Nicholls, R. J.; Perkins, J. M.; Grievson, E. M.; Theuwissen, K.; McComb, D. W.; Nellist, P. D.; Nicolosi, V., *Science* **2011**, 331, 568-571.
17. Hernandez, Y.; Nicolosi, V.; Lotya, M.; Blighe, F. M.; Sun, Z.; De, S.; McGovern, I. T.; Holland, B.; Byrne, M.; Gun'Ko, Y. K.; Boland, J. J.; Niraj, P.; Duesberg, G.; Krishnamurthy, S.; Goodhue, R.; Hutchison, J.; Scardaci, V.; Ferrari, A. C.; Coleman, J. N., *Nature Nanotechnology* **2008**, 3, 563-568.
18. Barwich, S.; Khan, U.; Coleman, J. N., *The Journal of Physical Chemistry C* **2013**.
19. Blake, P.; Brimicombe, P. D.; Nair, R. R.; Booth, T. J.; Jiang, D.; Schedin, F.; Ponomarenko, L. A.; Morozov, S. V.; Gleeson, H. n. F.; Hill, E. W.; Geim, A. K.; Novoselov, K. S., *Nano Letters* **2008**, 8, 1704-1708.
20. Choi, E. Y.; Choi, W. S.; Lee, Y. B.; Noh, Y. Y., *Nanotechnology* **2011**, 22.
21. Cui, X.; Zhang, C. Z.; Hao, R.; Hou, Y. L., *Nanoscale* **2011**, 3, 2118-2126.
22. Cunningham, G.; Lotya, M.; Cucinotta, C. S.; Sanvito, S.; Bergin, S. D.; Menzel, R.; Shaffer, M. S. P.; Coleman, J. N., *ACS Nano* **2012**, 6, 3468-3480.
23. Hernandez, Y.; Lotya, M.; Rickard, D.; Bergin, S. D.; Coleman, J. N., *Langmuir* **2010**, 26, 3208-3213.
24. Khan, U.; O'Neill, A.; Lotya, M.; De, S.; Coleman, J. N., *Small* **2010**, 6, 864-871.
25. Li, J. T.; Ye, F.; Vaziri, S.; Muhammed, M.; Lemme, M. C.; Ostling, M., *Carbon* **2012**, 50, 3113-3116.
26. Lin, Y.; Williams, T. V.; Connell, J. W., *Journal of Physical Chemistry Letters* **2010**, 1, 277-283.
27. Lin, Y.; Williams, T. V.; Xu, T. B.; Cao, W.; Elsayed-Ali, H. E.; Connell, J. W., *Journal of Physical Chemistry C* **2011**, 115, 2679-2685.
28. O'Neill, A.; Khan, U.; Coleman, J. N., *Chem. Mater.* **2012**, 24, 2414-2421.

29. Warner, J. H.; Rummeli, M. H.; Bachmatiuk, A.; Buchner, B., *Acs Nano* **2010**, 4, 1299-1304.
30. Zhi, C. Y.; Bando, Y.; Tang, C. C.; Kuwahara, H.; Golberg, D., *Advanced Materials* **2009**, 21, 2889-+.
31. Zhou, K. G.; Mao, N. N.; Wang, H. X.; Peng, Y.; Zhang, H. L., *Angewandte Chemie-International Edition* **2011**, 50, 10839-10842.
32. Yi, M.; Shen, Z. G.; Ma, S. L.; Zhang, X. J., *Journal of Nanoparticle Research* **2012**, 14.
33. Green, A. A.; Hersam, M. C., *Nano Letters* **2009**, 9, 4031-4036.
34. Lotya, M.; Hernandez, Y.; King, P. J.; Smith, R. J.; Nicolosi, V.; Karlsson, L. S.; Blighe, F. M.; De, S.; Wang, Z. M.; McGovern, I. T.; Duesberg, G. S.; Coleman, J. N., *Journal of the American Chemical Society* **2009**, 131, 3611-3620.
35. Smith, R. J.; King, P. J.; Lotya, M.; Wirtz, C.; Khan, U.; De, S.; O'Neill, A.; Duesberg, G. S.; Grunlan, J. C.; Moriarty, G.; Chen, J.; Wang, J. Z.; Minett, A. I.; Nicolosi, V.; Coleman, J. N., *Advanced Materials* **2011**, 23, 3944-+.
36. Vadukumpully, S.; Paul, J.; Valiyaveetil, S., *Carbon* **2009**, 47, 3288-3294.
37. Bourlinos, A. B.; Georgakilas, V.; Zboril, R.; Steriotis, T. A.; Stubos, A. K.; Trapalis, C., *Solid State Communications* **2009**, 149, 2172-2176.
38. May, P.; Khan, U.; Hughes, J. M.; Coleman, J. N., *Journal of Physical Chemistry C* **2012**, 116, 11393-11400.
39. Hughes, J. M.; Aherne, D.; Coleman, J. N., *Journal of Applied Polymer Science* **2013**, 127, 4483-4491.
40. May, P.; Khan, U.; O'Neill, A.; Coleman, J. N., *Journal of Materials Chemistry* **2012**, 22, 1278-1282.
41. Khan, U.; May, P.; O'Neill, A.; Bell, A. P.; Boussac, E.; Martin, A.; Semple, J.; Coleman, J. N., *Nanoscale* **2013**, 5, 581-587.
42. Wang, J. Z.; Lu, L.; Lotya, M.; Coleman, J. N.; Chou, S. L.; Liu, H. K.; Minett, A. I.; Chen, J., *Advanced Energy Materials* **2013**, 3, 798-805.
43. Cunningham, G.; Khan, U.; Backes, C.; Hanlon, D.; McCloskey, D.; Donegan, J. F.; Coleman, J. N., *Journal of Materials Chemistry C* **2013**, DO I: 10.1039 /c3tc314 02b.
44. Li, J.; Ye, F.; Vaziri, S.; Muhammed, M.; Lemme, M. C.; Östling, M., *Advanced Materials* **2013**, 25, 3985-3992.
45. Ma, R. Z.; Sasaki, T., *Advanced Materials* **2010**, 22, 5082-5104.
46. Hu, B.; Mai, L.; Chen, W.; Yang, F., *ACS Nano* **2009**, 3, 478-482.
47. Kalantar-zadeh, K.; Tang, J.; Wang, M.; Wang, K. L.; Shailos, A.; Galatsis, K.; Kojima, R.; Strong, V.; Lech, A.; Wlodarski, W.; Kaner, R. B., *Nanoscale* **2010**, 2, 429-433.
48. Andersson, G.; Magneli, A., *Acta Chemica Scandinavica* **1950**, 4, 793-797.
49. Scanlon, D. O.; Watson, G. W.; Payne, D. J.; Atkinson, G. R.; Egdell, R. G.; Law, D. S. L., *The Journal of Physical Chemistry C* **2010**, 114, 4636-4645.
50. Mendoza-Sanchez, B.; Brousse, T.; Ramirez-Castro, C.; Nicolosi, V.; Grant, P. S., *Electrochimica Acta* **2013**, 91, 253-260.
51. Murugan, A. V.; Viswanath, A. K.; Gopinath, C. S.; Vijayamohanan, K., *Journal of Applied Physics* **2006**, 100.
52. Brezesinski, T.; Wang, J.; Tolbert, S. H.; Dunn, B., *Nat Mater* **2010**, 9, 146-151.
53. Riley, L. A.; Lee, S.-H.; Gedvilias, L.; Dillon, A. C., *Journal of Power Sources* **2010**, 195, 588-592.
54. Gao, B.; Fan, H.; Zhang, X., *Journal of Physics and Chemistry of Solids* **2012**, 73, 423-429.
55. Li, W.; Cheng, F.; Tao, Z.; Chen, J., *The Journal of Physical Chemistry B* **2005**, 110, 119-124.
56. Tsumura, T.; Inagaki, M., *Solid State Ionics* **1997**, 104, 183-189.
57. Tao, T.; Glushenkov, A. M.; Zhang, C. F.; Zhang, H. Z.; Zhou, D.; Guo, Z. P.; Liu, H. K.; Chen, Q. Y.; Hu, H. P.; Chen, Y., *Journal of Materials Chemistry* **2011**, 21, 9350-9355.
58. Hildebrand, J. H.; Prausnitz, J. M.; Scott, R. L., *Regular and related solutions*. First ed.; Van Nostrand Reinhold Company: New York, 1970; p 228.
59. Ruoff, R. S.; Tse, D. S.; Malhotra, R.; Lorents, D. C., *Journal of Physical Chemistry* **1993**, 97, 3379-3383.

60. Hughes, J. M.; Hernandez, Y.; Aherne, D.; Doessel, L.; Mullen, K.; Moreton, B.; White, T. W.; Partridge, C.; Costantini, G.; Shmeliov, A.; Shannon, M.; Nicolosi, V.; Coleman, J. N., *Journal of the American Chemical Society* **2012**, 134, 12168-12179.
61. Bergin, S. D.; Sun, Z. Y.; Rickard, D.; Streich, P. V.; Hamilton, J. P.; Coleman, J. N., *ACS Nano* **2009**, 3, 2340-2350.
62. Panayiotou, C., *Journal of Chemical Thermodynamics* **2012**, 51, 172-189.
63. Shih, C. J.; Lin, S. C.; Strano, M. S.; Blankschtein, D., *Journal of the American Chemical Society* **2010**, 132, 14638-14648.
64. Yi, M.; Shen, Z. G.; Zhang, X. J.; Ma, S. L., *Journal of Physics D-Applied Physics* **2013**, 46.
65. Cheng, Q. H.; Debnath, S.; Gregan, E.; Byrne, H. J., *Journal of Physical Chemistry C* **2008**, 112, 20154-20158.
66. Cheng, Q. H.; Debnath, S.; O'Neill, L.; Hedderman, T. G.; Gregan, E.; Byrne, H. J., *Journal of Physical Chemistry C* **2010**, 114, 4857-4863.
67. Detriche, S.; Zorzini, G.; Colomer, J. F.; Fonseca, A.; Nagy, J. B., *Journal of Nanoscience and Nanotechnology* **2008**, 8, 6082-6092.
68. Bergin, S. D.; Nicolosi, V.; Streich, P. V.; Giordani, S.; Sun, Z. Y.; Windle, A. H.; Ryan, P.; Niraj, N. P. P.; Wang, Z. T. T.; Carpenter, L.; Blau, W. J.; Boland, J. J.; Hamilton, J. P.; Coleman, J. N., *Advanced Materials* **2008**, 20, 1876+.
69. Hughes, J. M.; Aherne, D.; Bergin, S. D.; O'Neill, A.; Streich, P. V.; Hamilton, J. P.; Coleman, J. N., *Nanotechnology* **2012**, 23.
70. O'Neill, A.; Khan, U.; Coleman, J. N., *Chemistry of Materials* **2012**, 24, 2414-2421.
71. Nicolosi, V.; Vrbancic, D.; Mrzel, A.; McCauley, J.; O'Flaherty, S.; McGuinness, C.; Compagnini, G.; Mihailovic, D.; Blau, W. J.; Coleman, J. N., *Journal of Physical Chemistry B* **2005**, 109, 7124-7133.
72. O'Neill, A.; Khan, U.; Nirmalraj, P. N.; Boland, J.; Coleman, J. N., *Journal of Physical Chemistry C* **2011**, 115, 5422-5428.
73. Khan, U.; Porwal, H.; O'Neill, A.; Nawaz, K.; May, P.; Coleman, J. N., *Langmuir* **2011**, 27, 9077-9082.
74. Lucas, A.; Zakri, C.; Maugey, M.; Pasquali, M.; van der Schoot, P.; Poulin, P., *Journal of Physical Chemistry C* **2009**, 113, 20599-20605.
75. Lee, C.; Wei, X. D.; Kysar, J. W.; Hone, J., *Science* **2008**, 321, 385-388.
76. Bertolazzi, S.; Brivio, J.; Kis, A., *Acs Nano* **2011**, Article ASAP.
77. Schreiber, H. P.; Tewari, Y. B.; Wertheimer, M. R., *Journal of Applied Polymer Science* **1976**, 20, 2663-2673.
78. Khan, U.; O'Neill, A.; Porwal, H.; May, P.; Nawaz, K.; Coleman, J. N., *Carbon* **2012**, 50, 470-475.
79. Wang, Y.; Zhu, Y.; Xing, Z.; Qian, Y., *Int. J. Electrochem. Sci.* **2013**, 8, 9851-9857.
80. Klinbumrung, A.; Thongtem, T.; Thongtem, S., *Journal of Nanomaterials* **2012**, 2012.
81. Chen, Y.; Lu, C.; Xu, L.; Ma, Y.; Hou, W.; Zhu, J.-J., *CrystEngComm* **2010**, 12, 3740-3747.
82. Backes, C.; Smith, R. J.; McEvoy, N.; Berner, N. C.; Nerl, H. C.; O'Neill, A.; King, P.; Higgins, T.; Hanlon, D.; McCloskey, D.; Donegan, J. F.; Scheuschner, N.; Maultzsch, J.; Duesberg, G. S.; Nicolosi, V.; Coleman, J. N., *Nature Communications* **2014**, under review.
83. Dieterle, M.; Weinberg, G.; Mestl, G., *Physical Chemistry Chemical Physics* **2002**, 4, 812-821.
84. Camacho-López, M. A.; Escobar-Alarcón, L.; Picquart, M.; Arroyo, R.; Córdoba, G.; Haro-Poniatowski, E., *Optical Materials* **2011**, 33, 480-484.
85. Atuchin, V. V.; Gavrilova, T. A.; Kostrovsky, V. G.; Pokrovsky, L. D.; Troitskaia, I. B., *Inorganic Materials* **2008**, 44, 622-627.
86. Coquet, R.; Willock, D. J., *Physical Chemistry Chemical Physics* **2005**, 7, 3819-3828.
87. Queeney, K. T.; Friend, C. M., *The Journal of Physical Chemistry B* **1999**, 104, 409-415.
88. Navas, I.; Vinodkumar, R.; Lethy, K. J.; Detty, A. P.; Ganesan, V.; Sathe, V.; Pillai, V. P. M., *Journal of Physics D: Applied Physics* **2009**, 42, 175305.

89. Navas, I.; Vinodkumar, R.; Detty, A. P.; Mahadevan Pilla, V. P. In *Intense Photoluminescence From Nanostructured MoO₃ Films*, ICOP 2009-International Conference on Optics and Photonics, Chandigarh, India, 2009; Chandigarh, India, 2009.
90. Deb, S. K.; Chopoorian, J. A., *Journal of Applied Physics* **1966**, 37, 4818-4825.
91. Navas, I.; Vinodkumar, R.; Mahadevan Pillai, V. P., *Applied Physics A* **2011**, 103, 373-380.
92. Balendhran, S.; Deng, J.; Ou, J. Z.; Walia, S.; Scott, J.; Tang, J.; Wang, K. L.; Field, M. R.; Russo, S.; Zhuiykov, S.; Strano, M. S.; Medhekar, N.; Sriram, S.; Bhaskaran, M.; Kalantar-zadeh, K., *Advanced Materials* **2013**, 25, 109-114.
93. Labanowska, M., *Physical Chemistry Chemical Physics* **1999**, 1, 5385-5392.
94. Song, J.; Ni, X.; Zhang, D.; Zheng, H., *Solid State Sciences* **2006**, 8, 1164-1167.
95. Cunningham, G.; Lotya, M.; McEvoy, N.; Duesberg, G. S.; van der Schoot, P.; Coleman, J. N., *Nanoscale* **2012**, 4, 6260-6264.
96. Zhao, X.; Sanchez, B. M.; Dobson, P. J.; Grant, P. S., *Nanoscale* **2011**, 3, 839-855.
97. Mendoza-Sánchez, B.; Grant, P. S., *Electrochimica Acta* **2013**, 98, 294-302.
98. Conway, B. E., *Electrochemical Supercapacitors: Scientific Fundamental and Technological Applications*. Kluwer Academic/ Plenum Publishers: London, UK, 1999.
99. Oyerinde, O. F.; Weeks, C. L.; Anbar, A. D.; Spiro, T. G., *Inorganica Chimica Acta* **2008**, 361, 1000-1007.
100. Wells, A. F., *Structural Inorganic Chemistry*. Oxford University Press, USA: 1984; Vol. 5th edition.
101. Smith, R. L.; Rohrer, G. S., *Journal of Solid State Chemistry* **1996**, 124, 104-115.
102. Bose, S.; Kuila, T.; Mishra, A. K.; Rajasekar, R.; Kim, N. H.; Lee, J. H., *Journal of Materials Chemistry* **2012**, 22, 767-784.
103. Dong, X. C.; Wang, X. W.; Wang, L.; Song, H.; Li, X. G.; Wang, L. H.; Chan-Park, M. B.; Li, C. M.; Chen, P., *Carbon* **2012**, 50, 4865-4870.
104. Kim, J. H.; Lee, K. H.; Overzet, L. J.; Lee, G. S., *Nano Letters* **2011**, 11, 2611-2617.
105. Li, S. M.; Wang, Y. S.; Yang, S. Y.; Liu, C. H.; Chang, K. H.; Tien, H. W.; Wen, N. T.; Ma, C. C. M.; Hu, C. C., *Journal of Power Sources* **2013**, 225, 347-355.
106. Liu, Y.; Huang, H. W.; Peng, X. S., *Electrochimica Acta* **2013**, 104, 289-294.
107. Wang, X. F.; Wang, D. Z.; Liang, J., *Chinese Journal of Inorganic Chemistry* **2003**, 19, 137-141.
108. Stauffer, D.; Aharony, A., *Introduction to Percolation Theory*. 2nd ed.; Taylor & Francis: London, 1985.
109. Bauhofer, W.; Kovacs, J. Z., *Composites Science and Technology* **2009**, 69, 1486-1498.
110. Zhao, X.; Johnston, C.; Grant, P. S., *Journal of Materials Chemistry* **2009**, 19, 8755-8760.
111. Zhao, X.; Johnston, C.; Crossley, A.; Grant, P. S., *Journal of Materials Chemistry* **2010**, 20, 7637-7644.
112. Qu, Q.; Zhang, P.; Wang, B.; Chen, Y.; Tian, S.; Wu, Y.; Holze, R., *The Journal of Physical Chemistry C* **2009**, 113, 14020-14027.
113. Huang, Q.; Wang, X.; Li, J., *Electrochimica Acta* **2006**, 52, 1758-1762.
114. Celzard, A.; McRae, E.; Deleuze, C.; Dufort, M.; Furdin, G.; Mareche, J. F., *Physical Review B* **1996**, 53, 6209-6214.
115. Wu, Z. C.; Chen, Z. H.; Du, X.; Logan, J. M.; Sippel, J.; Nikolou, M.; Kamaras, K.; Reynolds, J. R.; Tanner, D. B.; Hebard, A. F.; Rinzler, A. G., *Science* **2004**, 305, 1273-1276.



ToC fig